Vlasov Simulations of Thermal Plasma Waves with Relativistic Phase Velocity in a Lorentz Boosted Frame

A. G. R. Thomas[1, 2, 3, 4]

[1]*Center for Ultrafast Optical Science, University of Michigan, Ann Arbor, Michigan 48109, USA*
[2]*Department of Nuclear Engineering and Radiological Sciences, University of Michigan, Ann Arbor, Michigan 48109, USA*
[3]*Department of Physics, University of Michigan, Ann Arbor, Michigan 48109, USA*
[4]*Physics Department, Lancaster University, Bailrigg, Lancaster LA1 4YW, USA*

(Dated: September 7, 2016)

For certain classes of relativistic plasma problems, performing numerical calculations in a Lorentz boosted frame can be even more advantageous for gridded momentum-space-time (e.g. Vlasov) problems than has been demonstrated for position space-time problems and result in a potential reduction in the number of calculations needed by a factor $\sim \gamma_b^6$. In this study, the Lorentz boosted frame technique was applied to the problem of warm wavebreaking limits of plasma waves with relativistic phase velocity. The numerical results are consistent with analytic conclusions. By appropriate normalization and for sufficiently warm plasma, the dynamics for the Vlasov equation in different Lorentz frames were found to be independent of γ_p.

I. INTRODUCTION

Plasma based accelerators [1–5] show much promise as an advanced accelerator concept due to their very high acceleration gradients. Low-noise Eulerian-Vlasov simulations may be of interest for understanding the effect of the initial thermal distribution on particle trapping and wave amplitude [6]. Simulations of relativistic phase velocity waves in thermal laboratory plasmas, such as those relating to laser or beam driven plasma wakefield accelerator experiments [7–9], are, however, constrained by the fact that the maximum and minimum momenta that need to be resolved, in the direction of propagation, have a large difference in magnitude.

For a non-evolving driver, the maximum possible forward momentum gain in a plasma accelerator scales as the Lorentz factor associated with the phase velocity of the plasma wave, γ_p, squared, $p_{max} \propto \gamma_p^2 mc$ whereas the initial momentum spread, p_{th}, corresponding to the square root of the plasma temperature, is extremely small, $p_{th} \ll mc$. Even if initially the unperturbed plasma is relatively warm, a 100 eV plasma for example, then the momentum spread is $p_{th} \sim 10^{-2} mc$, which is very small compared with the maximum momentum, $p_{max} \gg mc$. This means to resolve the smallest and largest scales, for a numerical solution on a mesh, the number of grid points required in momentum space, N_p is enormous. For example, consider laser wakefield acceleration [10] in a 100 eV plasma with a 1 GeV energy gain; the minimum number of momentum grid points required to minimally resolve these disparate scales is $N_p \sim 10^5$, which is computationally intensive when combined with spatiotemporal dependence, even in 1D1P geometry. For a beam driven plasma wakefield, due to drive beam limitations the maximum energy does not scale as γ_p^2, but the energy of the accelerated particles is typically very large compared with the thermal spread anyway.

In this paper, we investigate the use of Eulerian-Vlasov simulations using a Fourier based code in a Lorentz boosted frame for studies of relativistic phase velocity perturbations in thermal plasma. In section II we discuss how, because of the noninvariance of energy-momentum scales in Eulerian-Vlasov finite-difference-time-domain simulations, performing the simulation in a boosted frame can lead to dramatic speed-ups in calculation time, as an extension of the space-time considerations of Vay [11]. Then, in section III, we make use of this technique to allow a numerical investigation into the maximum electric field achievable in a plasma wave with relativistic phase velocity (the "warm wavebreaking threshold"). This is compared with the results of a recent analytic study. Finally, several appendices describe the numerical scheme for the Vlasov code used in this study and its verification.

Unless otherwise stated, a system of units normalized to *laboratory frame reference plasma quantities* appropriate to relativistic plasma is used throughout; $v \to v/c$, $x \to x\omega_p/c$, $t \to \omega_p t$, $p \to p/mc$, $E \to qE/mc\omega_p$, $\rho \to \rho/\rho_0$ etc., where $\omega_p = \sqrt{q\rho_0/m\epsilon_0}$ is the plasma frequency for a neutralized species of charge q, mass m and charge density ρ_0. The fact that *all* variables (i.e. even those in the boosted frame) are normalized to laboratory frame quantities is important later on when discussing the similarity of solutions in the boosted frame.

II. VLASOV COMPUTATION IN A BOOSTED FRAME

The use of a Lorentz boosted frame to speed up plasma based wakefield acceleration calculations in particle-in-cell simulations is well known in the literature [11–13]. The advantage in this approach is that by boosting to a frame co-propagating with the relativistically moving object at wake phase Lorentz factor γ_p, the smallest time/space scales that need to be resolved (e.g. the laser

period) become larger since they copropagate with the boost, but the plasma length that needs to be integrated over shrinks due to Lorentz contraction. Hence, the number of calculations needed to resolve the simulation is greatly reduced. A Lorentz boosted frame has also been applied in the direction perpendicular to one dimensional (in space) Eulerian-Vlasov simulations to enable the simulation of a laser pulse with oblique incidence [14].

The covariant form of the Vlasov equation is [15]

$$\left(p_\mu \frac{\partial}{\partial x_\mu} + F^{\alpha\mu} p_\mu \frac{\partial}{\partial p^\alpha}\right) f_4(x,p) = 0 \,, \tag{1}$$

where p^ν is the four-momentum, x^ν the four-position, field tensor $F^{\alpha\mu} = \partial^\alpha A^\mu - \partial^\mu A^\alpha$ and $f_4(x,p)$ the particle distribution in $d^4x\, d^4p$. For numerical solutions of the relativistic Vlasov equation, due to desiring a fixed laboratory time interval for a time-stepping algorithm and the computational inefficiency of calculating the eight dimensional covariant form of the Vlasov equation, it is more convenient to use a numerical form of the non-invariant form of the Vlasov equation for distribution $f(\mathbf{x},\mathbf{p},t)$,

$$\frac{\partial f}{\partial t} + \frac{\mathbf{p}}{\sqrt{1+|\mathbf{p}|^2}} \cdot \frac{\partial f}{\partial \mathbf{x}} + \left(\mathbf{E} + \frac{\mathbf{p}}{\sqrt{1+|\mathbf{p}|^2}} \times \mathbf{B}\right) \cdot \frac{\partial f}{\partial \mathbf{p}} = 0 \,, \tag{2}$$

obtained by integrating Eqn. 1 with respect to p^0 using the relativistic energy-momentum relation and discretize in time, space and momentum space with fixed time/space/momentum step sizes $\Delta t/\Delta\mathbf{x}/\Delta\mathbf{p}$. It is also more typical to solve for fields $\mathbf{E}$ and $\mathbf{B}$ than A^μ in numerical calculations.

A. Vlasov simulations in a Lorentz-boosted frame

We start with the resolution required to resolve a function of x and t only, calculated on a regular Cartesian grid in different inertial frames. Consider the inertial frame O in which the number of grid points required to resolve all phenomena of interest in space and time are N_x and N_t respectively and *are the minimum required in any inertial frame of reference*. By assuming that there is a frame of reference in which the number of calculations required is minimized, we will then demonstrate that, by boosting to a different frame of reference, the number of calculations required to resolve the same physics is always increased.

We can relate the number of grid points to the extent of the simulation $L_x = x_2 - x_1$ and duration $L_t = t_2 - t_1$ that encompasses all phenomena of interest occuring between positions x_1 and x_2 and times t_1 and t_2. Define the uniform grid spacings Δx and Δt through $\Delta x = L_x/N_x$ and $\Delta t = L_t/N_t$. The total number of calculations over the whole space-time mesh is of order $N = N_x N_t$.

In a new frame O', related to O by a boost with Lorentz factor γ_p, we can find the new number of calculations N', assuming a uniform grid, through $N' = N'_x N'_t$, with $N'_x = L'_x/\Delta x'$ and $N'_t = L'_t/\Delta t'$.

The new extents of the simulation in the frame O', L'_x and L'_t and the new grid spacings, $\Delta x'$ and $\Delta t'$, can be related to extents and spacings in the frame O as follows. The left hand figure of Fig. 1 shows a bounded sinusoidal function in $x-t$ space representing some particular system of interest. The right hand figure shows the same system boosted with $\gamma_p = 1.25$. Note that the coordinate system is chosen so that the origin is at the center of the domain. When the system is sheared, assuming it is now modeled using a regular rectangular mesh, the new size of the simulation (maximum extent) must be $L'_x = \gamma_p\,(1 + v_p/v_L)\,L_x$, where $v_L = L_x/L_t$, by $L'_t = \gamma_p\,(1 + v_L v_p)\,L_t$, in size, for a boost with velocity $\pm v_p$.

To determine the resolution required in a new frame of reference, consider the Fourier decomposition of the function by wavenumber k_j and frequency ω_n, from $-k_{\max} \to k_{\max}$ and $-\omega_{\max} \to \omega_{\max}$. The limits of the Fourier-space can be related to the grid spacings by the Nyquist frequencies, $\Delta x < \pi/k_{\max}$ and $\Delta t < \pi/\omega_{\max}$. Using the transforms $k' = \gamma_p(k - v_p\omega)$ and $\omega' = \gamma_p(\omega - v_p k)$, in a new frame of reference there will be a new set of waves with wavenumbers k' and frequencies ω' representing the same physical behavior of interest. Therefore, in the new frame the largest wavenumber is $k'_{max} = \gamma_p(k_{max} + v_p\omega_{max})$ and the largest frequency is $\omega'_{max} = \gamma_p(\omega_{max} + v_p k_{max})$. By again relating the Nyquist frequencies to the grid spacings, $\Delta x' < \pi/k'_{\max}$ and $\Delta t' < \pi/\omega'_{\max}$, in the new frame of reference, we can relate Δx and Δt to $\Delta x'$ and $\Delta t'$ by

$$\Delta x' = \frac{\Delta x}{\gamma_p\,(1 + v_p v_\Delta)}$$

and

$$\Delta t' = \frac{\Delta t}{\gamma_p\,(1 + v_p/v_\Delta)} \,,$$

where $v_\Delta = \Delta x/\Delta t$. Hence,

$$N'_x = \gamma_p^2\,(1 + v_p/v_L)\,(1 + v_p v_\Delta)\,N_x$$

and

$$N'_t = \gamma_p^2\,(1 + v_p v_L)\,(1 + v_p/v_\Delta)\,N_t \,.$$

To perform the same calculation on a regular grid in the boosted frame, we must use the grid shown in the right hand panel of Fig. 1 as red dash-dot lines. If we additionally used a rectangular boundary, it would need to encompass the whole region including parts outside of the the domain of interest (black dashed line), since it is sheared in time and space. Clearly, the actual number of calculations can be reduced in this frame of reference, even for this regular rectangular mesh, by having a non-rectangular boundary. One example of this is the "moving box" technique in accelerator simulations [16]. Nevertheless, in general there is a substantial decrease

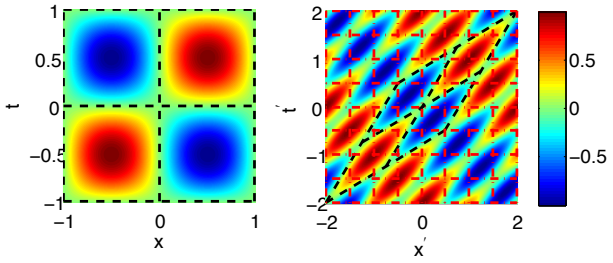

FIG. 1: (Left) A sinusoidal Lorentz scalar function in $x-t$ space. (Right) The same function in the frame boosted with $\gamma_p = 1.25$. The dashed black line indicates the domain of interest and grid required for resolving the function in the laboratory frame. The red dot-dashed lines indicate the rectangular grid required to resolve the function in the boosted frame.

in the number of calculations required in frame O compared with O'. For example, if we take $v_L = 1$, $v_\Delta = 1$, i.e. $\Delta x = \Delta t$ and $L_x = L_t$, then

$$N' = N'_x N'_t = \gamma_p^4 (1+v_p)^2 N \ .$$

That is to say, it is $\sim \gamma_p^2$ times faster to perform the calculation in the frame O. The analysis described above is basically equivalent to that described by Vay [11].

It turns out that there is a similarly beneficial effect for codes with a gridded momentum space. An example of this is solving the relativistic Vlasov equation, Eqn. 2, on a regular cuboid mesh. Consider a simulation with a uniform gridded momentum space in a Vlasov code in the frame O from $p_{min} = -p_0$ to $p_{max} = +p_0$, with grid step size Δp, that completely bounds the particle distribution. Note that this is the frame in which the momentum limits are symmetric, which will normally be the frame with the minimum number of calculations required (but not always). Similar to the spatial grid, the number of points on the momentum grid will be $N_p = L_p/\Delta p$, where $L_p = 2p_0$. In a new frame O', the momentum limits will be $p'_{min} = \gamma_p \left(-p_0 - v_p\sqrt{1+p_0^2}\right)$ and $p'_{max} = \gamma_p \left(p_0 - v_p\sqrt{1+p_0^2}\right)$, which means the extent of the momentum space increases by a factor of γ_p, i.e. $L'_p = \gamma_p L_p$.

After transformation, the required grid spacing in the new frame will depend on velocity, $\Delta p' = \gamma_p \left(\Delta p - v_p \Delta E\right) \simeq \gamma_p \left(1 - v_p v\right) \Delta p$. Assuming that to perform the simulation we still want to choose a uniform grid in the frame O', then the new grid spacing should be given by the smallest transformed grid cell,

$$\Delta p' = \gamma_p \left(1 - \frac{v_p p_0}{\sqrt{1+p_0^2}}\right) \Delta p \ .$$

Hence,

$$N'_p = \frac{N_p}{\left(1 - \frac{v_p p_0}{\sqrt{1+p_0^2}}\right)} \ .$$

If we consider a highly relativistic simulation, $p_0/\sqrt{1+p_0^2} \simeq 1$, then $N'_p \simeq N_p/(1-v_p) \simeq \gamma_p^2(1+v_p)N_p$.

For a full (1D1P) Vlasov simulation, the total number of calculations required is of order $N = N_x N_p N_t$. In general, the frame that minimizes the number of gridpoints $N_x N_t$ is not necessarily the same as the center of momentum frame O. However, for problems involving the crossing of two objects such as in plasma based accelerator schemes, free electron lasers etc., they do coincide [11]. This means that for such problems, the number of calculations required for a Vlasov simulation in a frame boosted in any direction *with respect to the optimum frame* O, i.e. O', scales as $N' \simeq \gamma_p^6 (1+v_p)^3 N$. Hence, if a simulation is performed in an optimum frame relative to, for example, a laboratory frame simulation, there may be an up-to γ_p^6 reduction in the number of calculations required depending on the situation. Fig. 2 illustrates this idea graphically. This result means that Vlasov simulations for plasma based accelerators under realistic conditions may be feasible.

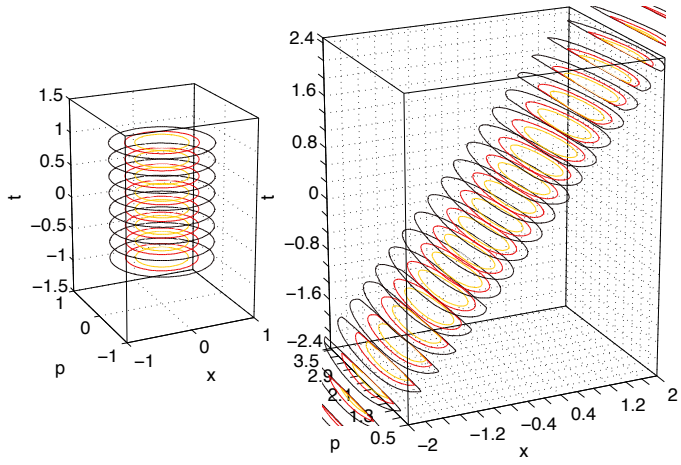

FIG. 2: (Left) A region of interest in $\{x, p, t\}$ space indicated by contours. (Right) The same region of interest in the frame boosted with $\gamma_p = 2$. The dotted lines on the walls indicate a characteristic grid size required for resolving the same physics in both boxes.

One other point of view is that instead of a Vlasov simulation, one may consider a simulation of wavefunctions of x, t but where there is a spread in k, ω. By an identical argument, the frame in which the frequency/wavenumber limits are symmetric will usually be optimal (since p, E can be replaced with k, ω).

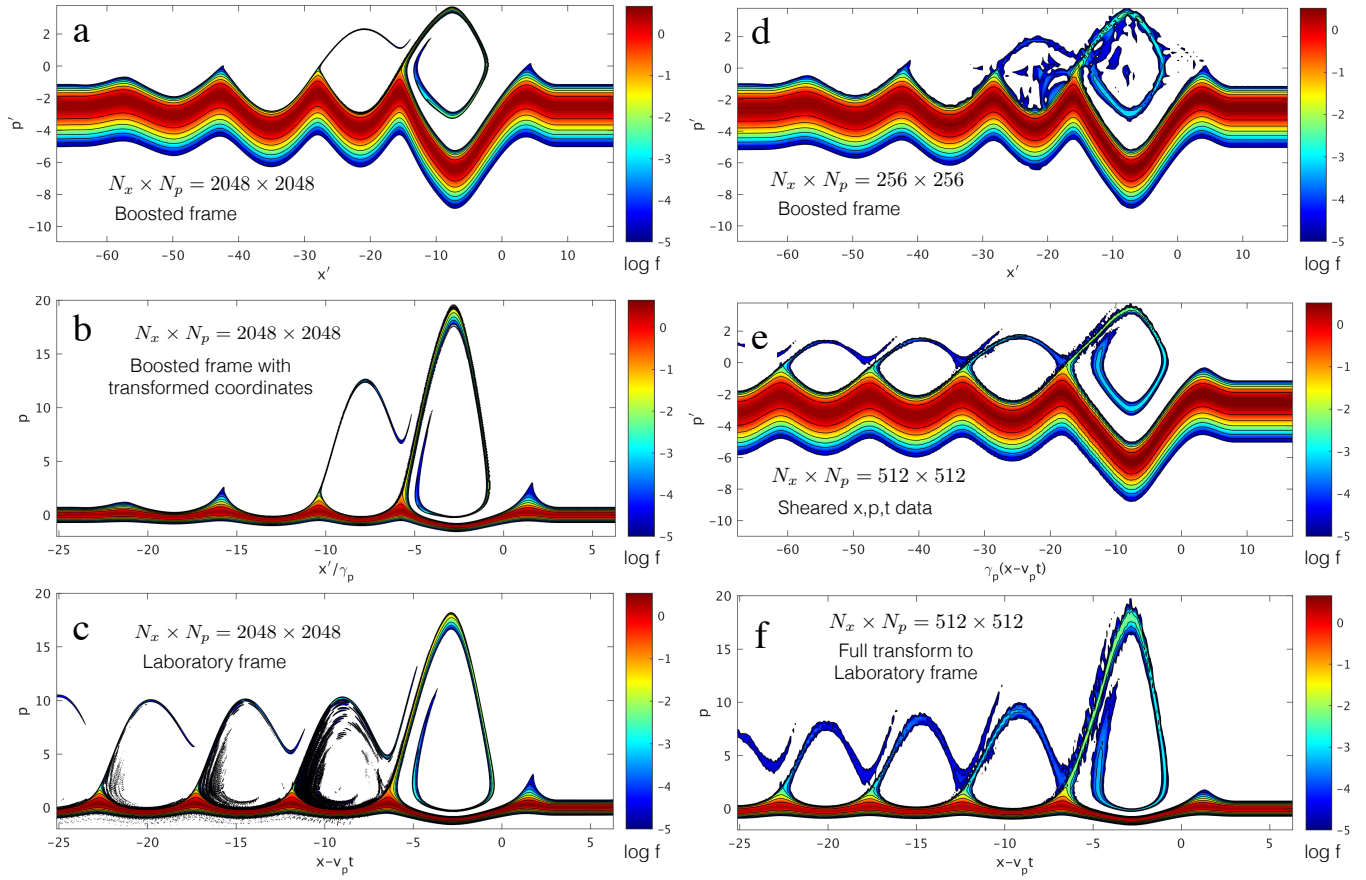

FIG. 3: Contour plots of the natural logarithm of distribution function f (with $x - v_p t/x'$ and p/p' scales cropped) for plasma wave simulations with a driver with $\gamma_p = \sqrt{7.25}$ in a plasma of normalized temperature $\theta = 0.04$. The driver is similar to that described in section III. All calculations are shown close to a laboratory frame time $t_f = 20\pi$. (a) Performed in a frame moving at v_p at slightly later than t_f. (b) shows the same calculation as (a), but displayed with transformed coordinates $p' \to p$ and $x' \to x - v_p t$. (c) The laboratory frame calculation at t_f. (d) The same boosted frame calculation as (a) but on a mesh with $64\times$ fewer gridpoints. (e) The same boosted frame calculation as (a) but on a courser mesh and transformed in x, t (as described in the main text) to $t = t_f$ in the laboratory frame. (f) Same as (e) but fully Lorentz transformed to the laboratory frame. The calculations were performed on different grids of $N_x \times N_p$ as indicated in the figure panels.

B. Thermal effects in plasma-based accelerators

Consideration of thermal effects are important in plasma-based accelerators [6] and an Eulerian-Vlasov method may be preferable to particle-based methods due to decreased noise. However, the former are very computationally intensive due to inefficient representation of the particle distribution. In a simulation of a laser wakefield accelerator in particular, the largest momentum that needs to be included on the momentum grid is the maximum forward momentum at dephasing $p_{max} \propto \gamma_p^2$ [10]. The minimum scale length to be resolved is the plasma momentum spread p_{th}, which is related to the plasma "temperature" $\theta m_e c^2 = k_B T$ (in real units). The difficulty is that $\theta \lll 1$ in any realistic scenario, such that the approximate number of grid points required is huge and scales unfavorably with γ_p, $p_{max}/\sqrt{2\theta} \propto \gamma_p^2 \ggg 1$. For example, consider a laser wakefield driver with Lorentz factor $\gamma_p = 30$ and a plasma temperature in real units of 100 eV $\simeq 2 \times 10^{-4} m_e c^2$. In this case, the minimum number of gridpoints required for a Vlasov simulation in the laboratory frame would be $\mathcal{O}\left(10^5\right)$.

In a frame boosted in the forward direction by γ_p, however, the new maximum momentum is

$$p'_{max} \simeq \left[\frac{1}{(1+v_p)\gamma_p} - \frac{\gamma_p v_p}{p_{max}^2}\right] p_{max} \ ,$$

i.e., p_{max} is reduced by a factor of $\mathcal{O}\left(\gamma_p\right)$. By contrast, the momentum spread $\sim \sqrt{\theta}$ of the plasma is increased.

Consider a symmetric distribution that has a characteristic width p_{th}, from $p_- = -p_{th}/2$ to $p_+ = +p_{th}/2$. The new momentum limits in the boosted frame are

$$p'_- = \gamma_p \left(p_- - v_p E_-\right) \ ,$$

$$p'_+ = \gamma_p \left(p_+ - v_p E_+\right) \ .$$

Since the width in the boosted frame is $p'_{th} = p'_+ - p'_-$, the energy terms cancel (for the symmetric limits considered) and hence

$$p'_{th} = \gamma_p p_{th} \ .$$

Therefore, in the boosted frame the ratio of the smallest momentum (the width) and the largest momentum (maximum forward momentum gain) that need to be resolved is decreased by a factor of γ_p^2, i.e. the number of momentum grid points can be reduced by a factor of γ_p^2, making calculations more tractable. For the wakefield example above, this would mean only $\mathcal{O}\left(10^2\right)$ momentum grid points required to resolve the same physics as in the laboratory frame.

To illustrate these scalings, Fig. 3 shows boosted frame and co-moving laboratory frame Vlasov simulations of a relativistically moving driver, reminiscent of the ponderomotive force of a laser, generating in its wake a plasma wave with relativistic phase velocity, in a plasma of normalized temperature $\theta = 0.04$. This driver is an external electric field. The precise simulation conditions are given later in section III and details of the Fourier based Vlasov code used for these calculations are given in the Appendices. The figure shows contour plots of the natural logarithm of distribution function f ($x - v_p t/x'$ and p/p' scales cropped) for plasma wave simulations with a driver with $\gamma_p = \sqrt{7.25}$. Contour plots are used here so that direct comparison of transformed distributions can be performed. All calculations are shown close to a laboratory frame time $t_f = 20\pi$. Fig. 3a is performed in a frame moving at v_p at slightly later than t_f. Fig. 3b shows the same calculation as (a), but displayed with transformed coordinates $p' \to p$ and $x' \to x - v_p t$. Fig. 3c shows the corresponding laboratory frame calculation at exactly t_f.

The time evolution of this structure in the two frames (boosted and laboratory) should clearly be different due to non-simultaneity of events. Since the laboratory frame plasma perturbation can be described in terms of the coordinates $\xi = x - v_p t$ and $\tau = t$, boosted frame time can be expressed as $t' = \gamma_p(\tau(1-v_p^2) - v_p\xi) = -\gamma_p v_p \xi + \tau/\gamma_p$. however and the absolute evolution is relatively slow, $\partial f/\partial\tau \ll \partial f/\partial\xi$, therefore time in the boosted frame will be dominated by the functional dependence on phase ξ. Fig. 3a and b are shown at a time t' such that at $x' = -2\pi$, the boosted frame time coincides with the laboratory frame time. Near to this point, when the space and momentum coordinates are transformed, the distribution function $f(x, p, t')$ looks similar, but not identical, to the real laboratory distribution $f(x, p, t)$ (this is not yet a proper Lorentz transform of the data).

The laboratory frame calculation in Fig. 3c shows errors at the $\log f = -3$ level despite the relatively large mesh (a-c are all calculated on a 2048×2048 grid with equivalent space/momentum limits). This is because the distribution is narrow relative to the momentum grid spacing ($p_{th}/\Delta p \approx 6$) and therefore the steep gradients cause errors in the Fourier representation. To show how the use of the boosted frame can speed up calculation, Fig. 3d shows the same boosted frame calculation as (a) but on a mesh with 64× fewer gridpoints (a 256×256 mesh). It shows errors at a level comparable with the fine mesh laboratory frame calculation Fig. 3 c, but the total simulation for Fig. 3d for $t_{max} = 48\pi$ took 42.8 s on a single 2.67 GHz Intel Xeon X5650 processor, whereas for Fig. 3a the calculation took $\approx$ 2617 s on the same processor. The laboratory frame calculations will not even complete on such a course mesh, but goes unstable because of the poor Fourier representation. For even slightly larger values of γ_p, it is not even possible to perform calculations in the laboratory frame with this serial code due to memory restrictions.

To properly compare calculations in the two inertial frames, a full Lorentz transform of $f'(x', p', t')$ must be performed. In practice this means recording the entire $f'(x', p', t')$ history and transforming the data volume, which requires a large amount of memory. With available resources transformation of the full $N_x \times N_p \times N_t = 2048 \times 2048 \times 757$ grid was not possible. However, simulations were also run in the boosted frame at $N_x \times N_p = 512 \times 512$ with a larger timestep of $\Delta t' = 0.5$, which allowed storage of the full $f'(x', p', t')$ data. This was then transformed by shifting the elements in the data cube in the time direction by a position vector dependent number $N_{shift}(x') = \text{floor}(N_t v_p x'/t_{max})$, which corresponds to $t' \to t' + v_p x'$, so that the transformed time corresponding to an (x', p') slice in the data volume is equivalent to a time $\gamma_p t$. Combined with Lorentz transformations of the space and momentum coordinates, the full Lorentz transformed distribution $f(x, p, t)$ can be constructed. Fig. 3e shows the same boosted frame calculation as (a) but on a courser mesh (512×512) and transformed in x, t as described above to coincide with $t = t_f$ in the laboratory frame. Finally, Fig. 3f shows the same data fully Lorentz transformed to the laboratory frame. It is now properly simultaneous to the real laboratory frame calculation Fig. 3c.

III. INVESTIGATION OF WARM WAVEBREAKING USING A LORENTZ BOOSTED FRAME

As an application of the technique described in the previous sections, we will examine the problem of warm wavebreaking of a wave with relativistic phase velocity v_ϕ, which has been studied by numerous authors [17–24] and for detailed discussion the reader is directed to those references. In particular, Schroeder et al [20] used relativistic fluid theory closed by neglecting centered moments of third order and higher, to indicate that for a thermal distribution in the limit $\gamma_p \to \infty$ (with $\gamma_p = \gamma_\phi = 1/\sqrt{1 - v_\phi^2}$ being associated with the phase velocity of the plasma wave in this case), the maximum electric field supported by a thermal plasma wave asymptotically approached a constant value, the value of which

they calculated. Here, a relativistic Vlasov numerical calculation in the frame boosted to where the wave phase velocity is zero will be directly applied to this problem as a demonstration; for the highest phase velocities investigated, to have the same effective resolution as the boosted frame calculations performed here the equivalent laboratory frame calculations would have to have $\mathcal{O}(10^3)$ times as many momentum grid points.

A. Similar dynamics of plasma in boosted frame

Before performing the simulations, we note that the 1D Vlasov-Maxwell system relevant to the warm wave-breaking of a plane wave can be written in the frame comoving with the plasma wave phase velocity using new further normalized coordinates $p' \to p'/\gamma_p$, $x' \to x'/\gamma_p$ and $t' \to t'/\gamma_p$. The resulting 1D Vlasov equation is

$$\frac{\partial f'}{\partial t'} + \frac{p'}{\sqrt{\frac{1}{\gamma_p^2} + p'^2}} \frac{\partial f'}{\partial x'} + E' \frac{\partial f'}{\partial p'} = 0 \,, \tag{3}$$

with $E' \to E'$ for consistency.

Gauss's law (see appendix VII for discussion of the use of Gauss's law / Ampère-Maxwell in 1D) is

$$\frac{\partial E'}{\partial x'} = \rho' - 1 \,, \tag{4}$$

where the charge density must be normalized as $\rho' \to \rho'/\gamma_p$ for consistency with the left hand side. The last term is 1 because the density is normalized to the laboratory frame reference density ρ_0, where the plasma is at rest. In the boosted frame this transforms to $\gamma_p \rho_0$ and therefore the normalized background density is 1. This definition is also consistent with

$$\rho' = \int_{-\infty}^{\infty} f' dp' \,, \tag{5}$$

with $f' \to f'$, which is satisfactory since the distribution is an invariant quantity.

Eqns (3–5) describe the self-consistent evolution of a Vlasov plasma in a frame boosted to velocity v_p. A plasma at rest in the laboratory frame with characteristic density $\rho_0 = 1$ and temperature θ (i.e. momentum spread $p_{th} = \sqrt{2\theta}$) will appear to be a plasma traveling with momentum $p_{drift} = -\gamma_p v_p$, density $\rho_0' = \gamma_p$ and momentum spread $\gamma_p\sqrt{2\theta}$ in the boosted frame in terms of the old variables. In the newly normalized set of variables, this becomes a plasma with momentum $p_{drift} = -v_p \simeq 1 - 1/2\gamma_p^2$, density $\rho_0' = 1$ and momentum spread $\sqrt{2\theta}$.

In the limit $\gamma_p^2 \to \infty$, there is no dependence on γ_p in Eqns (3–5) or the initial conditions. Therefore, the evolution of the normalized system should display similar dynamics for any $\gamma_p \gg 1$ for a given laboratory frame density ρ_0 and temperature θ. This is analogous to the similarity theory of Ref. [25], but with γ_p replacing the role of a_0 in that reference. There is a caveat to this; there will be a small region close to $p' = 0$ where the approximation $v' \simeq p'/|p'| = \pm 1$ breaks down. The width of this region is approximately $1/\gamma_p$. Therefore, provided the temperature of the plasma θ is such that $\gamma_p^2\theta \gg 1$, few particles will be in the region where the similar dynamics does not apply.

This analysis implies that the evolution of the warm plasma wave (with $\gamma_p^2\theta \gg 1$) should evolve with similar dynamics for any γ_p, regardless of any details of the distribution function shape in the limit $\gamma_p^2 \gg 1$ and therefore the maximum normalized electric field of the wave should not depend on γ_p. It does not, however, prescribe what that field strength is. Since the component of the electric field in the direction of the boost is invariant and the normalization of electric field does not depend on γ_p, the laboratory frame electric field must not depend on γ_p in this limit, but only on the temperature and plasma density, consistent with the results of Ref. [20].

The more general use of this similarity theory approach for scaling results from simulations of plasmas perturbed by relativistic objects will be addressed in a future publication.

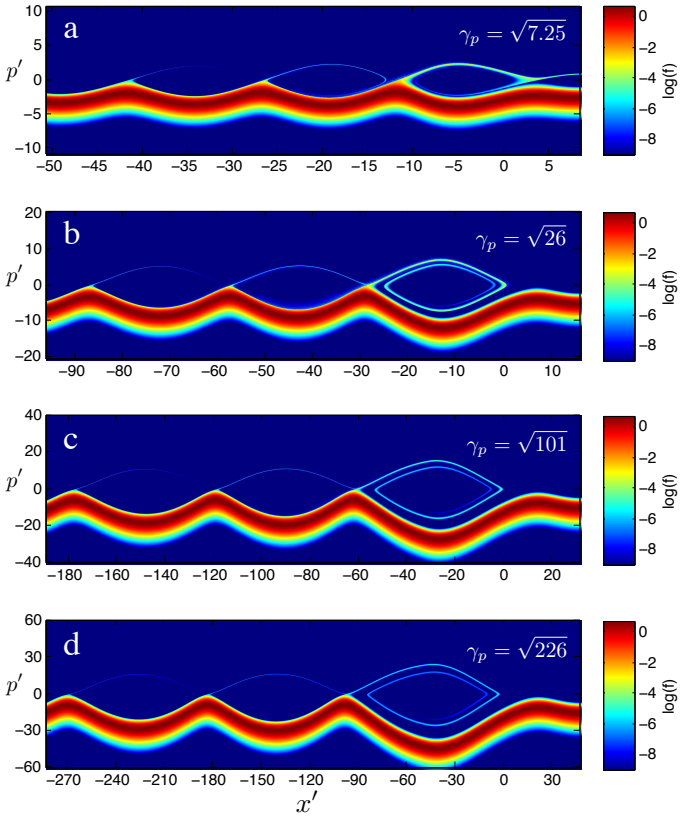

FIG. 4: Natural logarithm of distribution function f at $t' = 12\pi\gamma_p$ for different driver phase velocities; (a) $\gamma_p = \sqrt{7.25}$, (b) $\gamma_p = \sqrt{26}$, (c) $\gamma_p = \sqrt{101}$ and (d) $\gamma_p = \sqrt{226}$. The colorscale is truncated at the -9 level (i.e. for $f \lesssim 10^{-4}$, with maximum $f \simeq 2$).

B. Numerical simulations

To obtain the numerically calculated electric field strength for comparison with theory, we carried out simulations in the the frame in which the phase velocity of the wave is zero. This was necessary so that the thermal distribution with small spread and high energy electron acceleration were resolvable on a reasonable grid, as discussed in the previous sections. Simulations were carried out on a $N_x \times N_p = 2096 \times 2096$ uniform grid using the Fourier based Vlasov code described in Appendix VII. The time step was $\omega_p' \Delta t' = 0.2$ and the simulation proceeded until $t_{max} = 24\pi\gamma_p$. The initial distribution was a one dimensional drifting relativistic Maxwellian as described in Appendix VI with drifting momentum $-\gamma_p v_p$ and thermal spread $\theta = 0.04$. The domain length in x' was $14\gamma_p\pi$, defined in the range $x_{min} = -12\pi\gamma_p \leq x' \leq x_{max} = 2\pi\gamma_p$.

The maximum electric field supportable by the plasma wave was found by adding an external electric field (which could represent, for example a particle beam or the ponderomotive force of a laser driver). This field was increased slowly (with respect to the plasma period) in amplitude, monotonically from zero [26]. A plasma wave with increasing amplitude was consequently generated. The amplitude of the external field was increased in amplitude far beyond the point of saturation when the maximum plasma wave amplitude was reached and had a precise form;

$$E'_{x,ext} = \begin{cases} E_0(t')\cos(x'/\gamma_p) & \text{for } -\gamma_p\pi < x' < \gamma_p\pi \\ 0 & \text{otherwise} \end{cases} \tag{6}$$

where $E_0(t) = t'/t_{max}$, although *other functional forms were also tried, including a non-adiabatic drive (i.e. step function switch on), with similar results.*

At the ends of the domain, a equilibrating operator of the form $\partial f/\partial t'|_c = -\nu(x')\,[f - f_0]$ was added, where f_0 is the unperturbed initial distribution. This was because while the code has several nice properties with respect to conservation and accuracy, the calculation must be performed in a periodic domain due to the fast Fourier transform algorithm. The relativistic phase velocity waves generated do not, however, have a well defined period because their wavelength depends on the wave amplitude. The spatially dependent "collision frequency", $\nu(x')$, was zero within the domain of interest and had a sufficiently high value at the edges of the domain that the plasma streaming in from x_{max} was equal to f_0 to near machine precision before interacting with the externally applied electric field.

$$\nu(x') = 2\left[e^{-\left(\frac{x'-x_{max}}{\gamma_p\pi}\right)^{40}} + e^{-\left(\frac{x'-x_{min}}{\gamma_p\pi}\right)^{2}}\right].$$

Figure 4 shows snapshots in time of the distribution function at $t' = 12\pi\gamma_p$ into the simulation for 4 different phase velocities. The maximum and minimum momentum and space scales in each figure are deliberately set to multiples of γ_p to illustrate clearly the similar evolution of the distribution function as γ_p becomes large.

Fig. 5 shows various outputs from the code as a function of time t for a simulation with $\gamma_b = \sqrt{226}$. (a) and (b) show time histories of the density perturbation $\delta\rho'$ and electric field E'_x. The amplitude of the perturbation grows in time as the driving external electric field (not shown) increased. After reaching the maximum amplitude, the amplitude no longer grows, but instead the wavelength of the first period where the driver is situated increases, with the wave structure losing coherence.

Fig. 5 (c) shows the maximum of E'_x compared with the wavebreaking limit in Ref. [20], E_{SES}. The electric field amplitude grows smoothly until it approaches the wavebreaking limit, whereapon the field starts to oscillate due to fluctuations in the coherent structure of the wave, but no longer grows in amplitude on average. (d) shows the Fourier transform of $\delta\rho'$ as a function of wavenumber normalized to k'_p. As time progresses, we see the generation of harmonics of k_p as the wave becomes nonlinear and then subsequently the coherent structure of the wave starts to become lost.

Finally, Fig. 6 shows a comparison of the wavebreaking threshold from the analytic expression in Ref. [20] with the maximum electric field calculated by the Vlasov code for simulations over a range of values of γ_p for fixed θ. As can be seen from the figure, there is good agreement with the analytic expression over the range calculated to within the limitation of the fluctuations in the maximum field as the wave reaches maximum amplitude. The only discrepancy is at the lowest value of $\gamma_p^2\theta$, where the maximum field is much higher than the prediction. This is because so many particles are trapped as the simulation progresses that the assumptions in deriving the analytic expression are violated anyway.

IV. CONCLUSIONS

In conclusion, we have shown that using a boosted frame can be very advantageous for Vlasov simulations of relativistic thermal plasma waves. In the simulations performed here, at the highest value of $\gamma_p^2\theta$ with $\theta = 0.04$, therefore $\gamma_p = 50$. In the laboratory frame, trapped particles in the thermal distribution reach $\sim \gamma_p^2$ energy. Therefore the requirement on a uniform momentum grid minimally resolving the thermal distribution and overall dynamics would scale as $\sim \gamma_p^2/\theta \sim 10^5$ grid points, although for an accurate simulation it would be much higher than this. In the boosted frame with maximum/minimum momentum $\sim \gamma_p$ we require $\sim \gamma_p/\theta \sim 250$ grid points to minimally resolve the thermal distribution and overall dynamics (although an order of magnitude more than this were used for accurate results). The use of a boosted frame allowed the running of these simulations on a single processor in a relatively short time (a few hours for the longest).

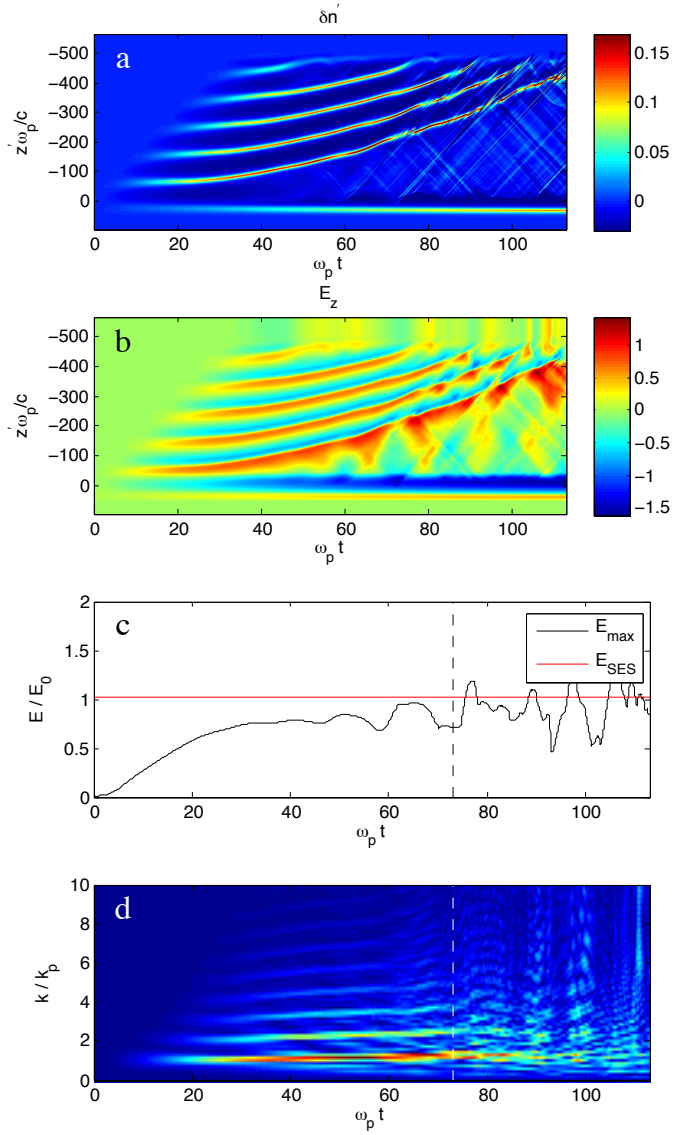

FIG. 5: Various outputs from the code as a function of time t for a simulation with $\gamma_b = \sqrt{226}$. (a) Density perturbation $\delta\rho'$, (b) electric field E_x, (c) maximum of E_x compared with the wavebreaking limit in Ref. [20], E_{SES} and (d) Fourier transform of $\delta\rho'$ as a function of wavenumber normalized to k'_p.

The use of a Lorentz boosted frame for Eulerian-Vlasov calculations should also be applicable to methods other than the Fourier solver used here. It should be noted, however, that numerical instabilities have been observed in particle-in-cell simulations using Lorentz boosted frames and various methods have been developed to mitigate them ([13] and references therein). For Eulerian-Vlasov calculations not using Fourier methods, as in this paper, similar methods would probably need to be applied also.

These simulations support the maximum electric field

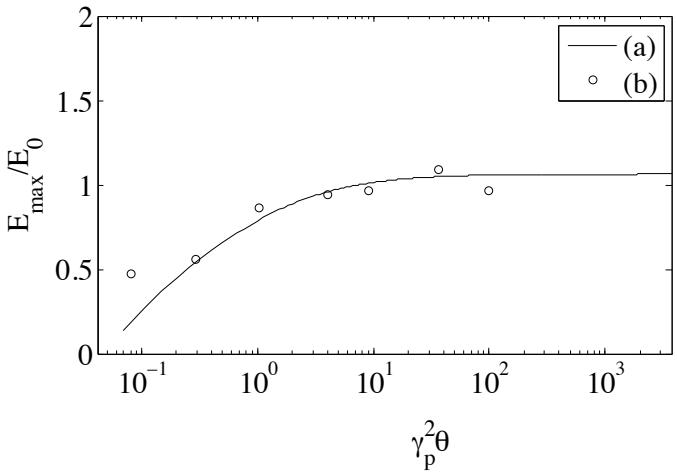

FIG. 6: Comparison of wavebreaking thresholds from (a) the analytic expression in Ref. [20] and (b) the maximum electric field calculated by the Vlasov code.

achievable calculated in Ref. [20], even under non-stationary conditions. When trapping of particles was sufficient to lead to a distribution with momentum spread that violated the assumptions in that model, the simulation results did not agree with the maximum electric field. The results of this paper also demonstrate evidence for the feasibility of Vlasov simulation for plasma based accelerator applications.

V. ACKNOWLEDGEMENTS

This material is based upon work supported by the Air Force Office of Scientific Research under award numbers FA9550-12-1-0310 (Young Investigator Program) and FA9550-14-1-0156 and the National Science Foundation Career grant 1054164.

VI. APPENDIX: 1D RELATIVISTIC DRIFTING MAXWELLIAN

For all the simulations performed in the boosted frame we must use a correctly initialized drifting relativistic Maxwellian ("Maxwell-Juttner") distribution in terms of only one momentum coordinate. In its rest frame, the relativistic Maxwellian with normalized temperature θ is [15]

$$f(\mathbf{p}_\perp, p) = \frac{1}{4\pi\theta K_2(1/\theta)} \exp\left[-\frac{1}{\theta}\sqrt{1+p_\perp^2+p^2}\right] ,$$

where $\mathbf{p}_\perp$ are the perpendicular (to the domain) components of the momentum and $K_2(x)$ is a modified Bessel function of the second kind. Since f is an invariant, we can express the distribution in the frame moving at v_p by

simply invoking the transform $\gamma = \gamma_p\,(\gamma' + v_p p')$. The 1D distribution can therefore be found by integrating over the transverse coordinates

$$f(p') = \frac{1}{4\pi\theta K_2(1/\theta)} \exp\left[-\frac{\gamma_p v_p p'}{\theta}\right] \times \int \exp\left[-\frac{\gamma_p}{\theta}\sqrt{1+p_\perp^2+p'^2}\right] d^2\mathbf{p}_\perp \,, \tag{7}$$

such that

$$f(p') = \frac{1}{2\gamma_p^2 K_2(1/\theta)} \left(\gamma_p\sqrt{1+p'^2}+\theta\right) \times \exp\left[-\frac{\gamma_p}{\theta}\left(\sqrt{1+p'^2}+v_p p'\right)\right] \,. \tag{8}$$

This distribution was used as the initial condition for the results in the main text. Note that in the limit that $\theta \to 0$, this expression reduces to

$$f(p') = \frac{\gamma_p^2}{\sqrt{2\pi\theta}} \exp\left[-\frac{(p'+\gamma_p v_p)^2}{2\gamma_p^2\theta}\right] \,,$$

which is a non-relativistic Maxwellian with a temperature γ_p^2 higher than in the plasma rest frame and shifted to a drifting momentum of $-\gamma_p v_p$ (and with density $\rho' = \int f(p')dp' = \gamma_p\rho$).

VII. APPENDIX: RELATIVISTIC SPECTRAL 1D1P VLASOV CODE

This appendix describes tests of the relativistic Fourier based 1D1P relativistic Vlasov code used in the studies in the previous sections, for verification and to demonstrate its numerical accuracy. Because it uses a Fourier based spectral method, it is ideal for studying periodic structures with high fidelity. There have been a number of different implementations of spectral and Fourier based schemes related to the one we develop here [27–32]. These often use Hermite polynomials for the expansion in momentum or velocity space, since the lowest order term is a Gaussian. Here, straightforward Fourier modes are used in both momentum and position space representations of the distribution $f(x,p,t)$. The Fourier-based method described here does not ensure positivity of the distribution f. Negative f can occur when gradients get sufficiently steep (insufficiently represented in Fourier space) that Gibbs phenomena occurs. A non-linear numerical diffusion operator is introduced in section VII A that preserves the steepness of gradients larger than a grid spacing but acts to smooth out ripples that would eventually lead to negative f. In all the tests here and the investigations in the rest of the manuscript the positivity of the distribution is monitored and numerical convergence checked. Here, we use the same dimensionless system of units as in the main section, $t \to \omega_p t$, $x \to x\omega_p/c$, $v \to v/c$, $\phi \to q\phi/mc^2$, $p \to p/mc$ etc. The Fourier Vlasov code used solves the two dimensional Vlasov equation (one spatial coordinate, one momentum coordinate)

$$\frac{\partial f}{\partial t} + v\frac{\partial f}{\partial x} + E\frac{\partial f}{\partial p} = 0 \,,$$

where f is the smooth one dimensional plasma distribution $f = \iint f_{3D} dp_y dp_z$,

$$v = \frac{p}{\sqrt{1+p^2}}$$

and E is the electric field arising from the scalar potential, which is solved for using Poisson's equation

$$-\nabla^2\phi = \rho - \rho_0 \,.$$

Note that the Vlasov-Poisson description that we use is not *generally* identical to the Vlasov-Maxwell, even in 1D, since the latter allows for a time dependent electric field $E_0(t)$ that is not constrained by the Poisson equation (Ampère-Maxwell being the time derivative of Poisson's equation in 1D, when combined with the continuity equation). This field is of the form $E_0(t) = (u_0 - U)\sin t + E_0(0)\cos t$ [33], where u_0 is the initial drift velocity of electrons, U is the drift velocity of the ions and $E_0(0)$ is the initial value of this time dependent only electric field. Since for all the problems we tackle, the initial electron and ion drift velocities are equal (the plasma is initially at rest in the laboratory frame), the plasma is initially exactly neutral and the initial external field is zero, $E_0(t) = 0$ for all times and therefore the Vlasov-Poisson and Vlasov-Maxwell systems are equivalent in 1D.

The distribution is represented by the gridded function f_{ij} where i denotes the index position on the x-grid spanning N_x points, x_i and j denotes the index of the p grid spanning N_p points, p_j. Δp is uniform, hence the difference between velocity cells, Δv, is not. To numerically solve this system of equations, the code uses an algorithm that splits the transport in the x and p directions [34, 35] to give overall second order accuracy in time. It uses discrete Fourier representations, given by

$$\tilde{f}_{ij} = \sum_{i'=0}^{N_x-1} f_{i'j} \exp\left[\frac{i_C 2\pi i i'}{N_x}\right]$$

and

$$\hat{f}_{ij} = \frac{1}{N_p}\sum_{j'=0}^{N_p-1} f_{ij'} \exp\left[-\frac{i_C 2\pi j j'}{N_p}\right]$$

and their respective inverse transforms, where $i_C = \sqrt{-1}$ and spaces k_i and κ_j, reciprocal to x_i and p_j. These are calculated using fast Fourier transforms. We use n to denote time step index via $t = n\Delta t$ with constant time step Δt.

There are four main steps:

1. The algorithm starts with the distribution function in reciprocal x space, $\tilde{f}_{ij}$. The algorithm pushes for a half step spatial advection via

$$\tilde{f}_{ij}^{n+1/2\star} = \tilde{f}_{ij}^{n} \exp\left[-i_C k_i v_j \frac{\Delta t}{2}\right] .$$

which is the solution to the oscillator (advection in real space) equation

$$\frac{\partial \tilde{f}}{\partial t} + i_C k v \tilde{f} = 0 .$$

2. Solve Poisson's equation to find the potential using the transformed charge density

$$\tilde{\rho}_i^{n+1/2} = \sum_{j=0}^{N_p-1} \tilde{f}_{ij}^{n+1/2\star} \Delta v$$

The numerical forms of Poisson's equation is

$$\tilde{\phi}_i^{n+1/2} = \frac{\tilde{\rho}}{k_i^2} .$$

The transformed force is calculated from $\tilde{F}_{x,i}^{n+1/2} = ik\phi^{n+1/2}$.

3. Perform a full two dimensional inverse transform Fourier transform $\tilde{f}_{ij} \rightarrow \hat{f}_{ij}$, i.e.

$$\hat{f}_{ij} = \frac{1}{N_x N_p} \sum_{j'=0}^{N_p-1} \sum_{i'=0}^{N_x-1} \tilde{f}_{i'j} \exp\left[-2\pi i_C \left(\frac{jj'}{N_p} + \frac{ii'}{N_x}\right)\right] ,$$

which returns the distribution to x space and transforms to reciprocal p space. Push for a full momentum space advection via

$$\hat{f}_{ij}^{n+1/2} = \hat{f}_{ij}^{n+1/2\star} \exp\left[-i_C \kappa_j F_i^{n+1/2} \Delta t\right] .$$

4. Perform a full two dimensional forward transform $\hat{f}_{ij} \rightarrow \tilde{f}_{ij}$ and finish with a half step spatial advection

$$\tilde{f}_{ij}^{n+1} = \tilde{f}_{ij}^{n+1/2} \exp\left[-i_C k_i v_j \frac{\Delta t}{2}\right] .$$

This algorithm is overall second order accurate with respect to the time step Δt, but exact with respect to the momentum and position space grids provided the Fourier representation of the function is accurate, i.e. system energy conservation, momentum conservation etc. does not depend on the Δp or Δx grid sizes. The stability condition is that of a standard second order scheme.

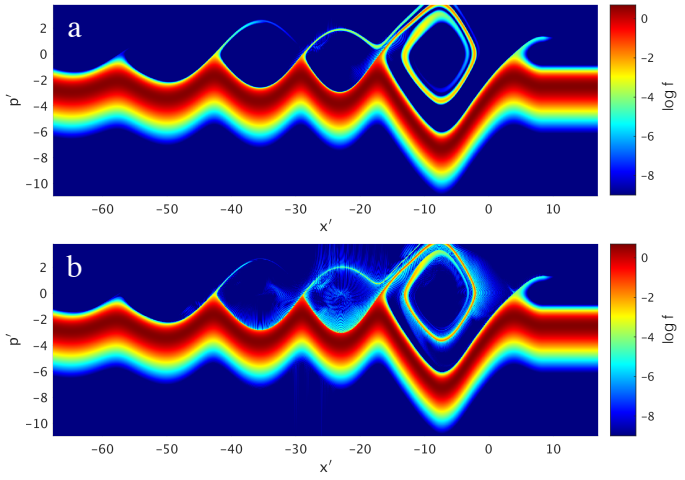

FIG. 7: Demonstration of the effect of nonlinear diffusion on the calculations described in the main text in section III. Calculations performed are on a $N_p \times N_x = 2048 \times 2048$ grid in the boosted frame. Both panels (a) and (b) show $\ln(f)$ under identical conditions except that in panel (a) a nonlinear diffusion operator with $D_0 = 0.5$ was applied.

A. Non-linear diffusion

The Fourier method for solving the Vlasov-Poisson equation detailed above may be inferior to other methods due to the steep gradients that lead to characteristic oscillating artifacts appearing. To mitigate this, introduction of numerical diffusion can smooth out ripples, but will also introduce diffusion of real sharp features in the distribution function. Instead, a nonlinear diffusion operator [36] was included in the calculations to smooth ripples but maintain steep gradients

$$f_{ij}^{\text{smooth}} = f_{ij} + \nabla_N \cdot (D_{ij} \nabla_N f_{ij}) \Delta t ,$$

where ∇_N is the numerical representation of the gradient operator, taken here to be standard second order center differenced and D_{ij} is a non-linear diffusion coefficient given by

$$D_{ij} = \frac{D_0}{1 + \frac{||\nabla_N f_{ij}||^2}{{f_{ij}}^2}} ,$$

where D_0 is a chosen linear diffusion coefficient.

The use of this is illustrated in Fig. 7, which shows calculations performed on a $N_p \times N_x = 2048 \times 2048$ grid in the boosted frame as described in the main text in section III. Both panels (a) and (b) show $\ln(f)$ under identical conditions except that in panel (a) a nonlinear diffusion operator with $D_0 = 0.5$ was applied. We can see that without the nonlinear diffusion filter, spectral errors start to appear starting at 10^{-3} of the maximum of f (which is actually quite reasonable anyway). However, with the nonlinear diffusion filter, panel (a), the spectral errors are negligible above 10^{-4} of the maximum of f and moreover the steep gradients in f are preserved.

B. Verification

A number of different tests and comparisons with code results from the literature were made with this code for verification. In this section just a couple of those performed are described, to demonstrate that the scheme has performance comparable to high-order schemes in the literature.

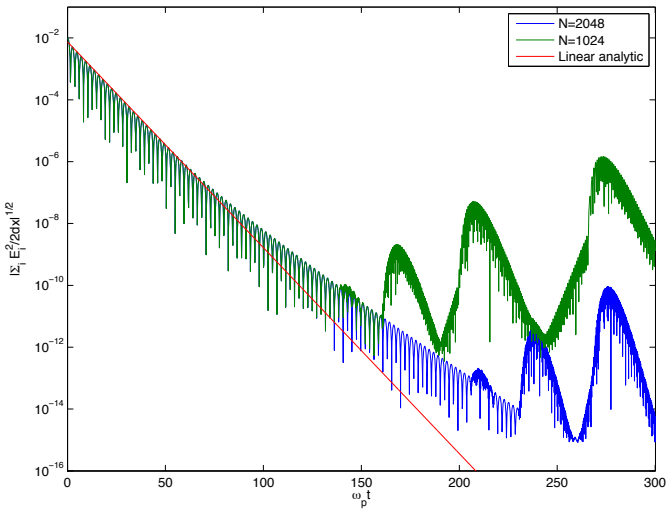

FIG. 8: Electric field energy $|\sum_i E_i^2 \Delta x/2|^{1/2}$ in the Landau damping problem described in the text for $N = 2048$ cells and $N = 1024$ cells.

1. Landau damping

This example simply demonstrates the accuracy of the method generally, for a nonrelativistic problem. The test problem is a standard Landau damping test [31], using a thermal plasma with an initial distribution specified as

$$f(x,p,t0) = \frac{1}{\sqrt{2\pi}} \exp\left(-\frac{p^2}{2}\right)\left[1 + 0.01\cos\left(\frac{x}{2}\right)\right] ,$$

with $x \in [0, 4\pi]$ and $v \in [-8, 8]$. The code is used in non-relativistic mode, so in this case $v = p$ instead of $\sqrt{1+p^2}$. The analytic damping rate is $\delta = 0.1533$. Fig. 8 shows the electric field energy as a function of time for $N_v = N_x = N = 2048$ cells and $N = 1024$ cells along with the linear decay solution. $\Delta t = 0.1$. The results in Fig. 8 are similar to those in reference [31], including the relatively large oscillations in electric field at late times.

2. Relativistic two-stream instability

The relativistic two stream instability is to verify the relativistic algorithm. The code is used in relativistic mode, so in this case $v = p/\sqrt{1+p^2}$. The test is a two stream instability, with an initial distribution function

$$f(x,p,t0) = \frac{1}{\sqrt{\pi}} \exp\left(-(|p| - p_0)^2\right)\left[1 + 10^{-10}\cos\left(k_{TS}x\right)\right] ,$$

with $p_0 = 3$,

$$k_{TS} = \frac{\sqrt{3\gamma}}{2p_0}$$

the wavenumber of the fastest growing mode, with growth-rate $\delta = \omega_p/2\sqrt{\gamma}$. The calculation was performed with $N_v = N_x = 2048$ and a time step of $\Delta t = 0.1$. Figure 9 shows the distribution at $t = 80$.

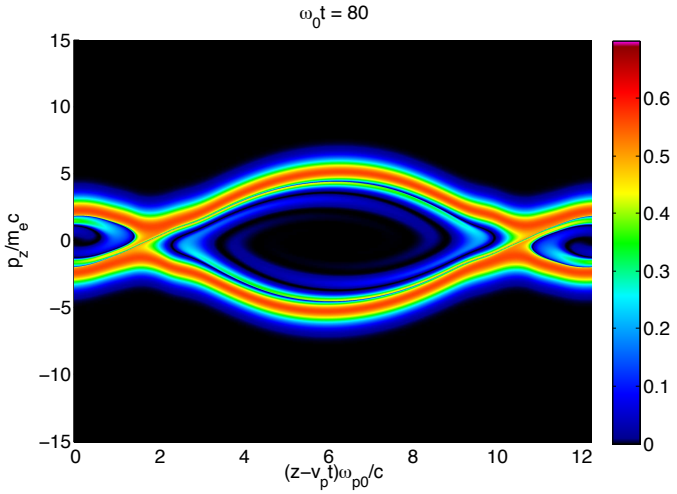

FIG. 9: Distribution function for the relativistic two stream instability.

Figure 10 shows the electric field energy as a function of time for the two stream instability cells along with the linear growth solution. Note that due to the initial perturbation being so small (10^{-10}) and the overall accuracy of the code, the growth is linear over approximately 8 orders of magnitude before saturating.

[1] S. P. D. Mangles, C. D. Murphy, Z. Najmudin, A. G. R. Thomas, J. L. Collier, A. E. Dangor, E. J. Divall, P. S. Foster, J. G. Gallacher, C. J. Hooker, et al., Nature **431**, 535 (2004).

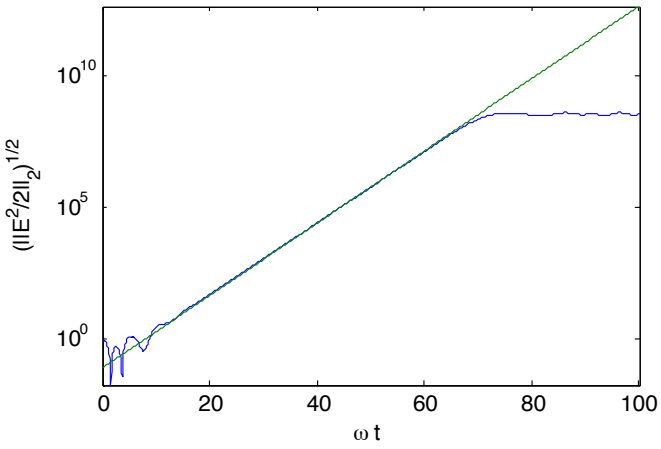

FIG. 10: (Blue line)Electric field energy $|\sum_i E_i^2 \Delta x/2|^{1/2}$ in the two stream problem described in the text. (Green line) Analytic solution.

[2] C. G. R. Geddes, C. Toth, J. V. Tilborg, E. Esarey, C. B. Schroeder, D. Bruhwiler, C. Nieter, J. Cary, and W. P. Leemans, Nature **431**, 538 (2004).

[3] J. Faure, Y. Glinec, A. Pukhov, S. Kiselev, S. Gordienko, E. Lefebvre, J.-P. Rousseau, F. Burgy, and V. Malka, Nature **431**, 541 (2004).

[4] I. Blumenfeld, C. E. Clayton, F.-J. Decker, M. J. Hogan, C. Huang, R. Ischebeck, R. Iverson, C. Joshi, T. Katsouleas, N. Kirby, et al., Nature **445**, 741 (2006).

[5] M. Litos, E. Adli, W. An, C. I. Clarke, C. E. Clayton, S. Corde, J. P. Delahaye, R. J. England, A. S. Fisher, J. Frederico, et al., Nature **515**, 92 (2014), URL http://dx.doi.org/10.1038/nature13882.

[6] E. Esarey, C. B. Schroeder, E. Cormier-Michel, B. A. Shadwick, C. G. R. Geddes, and W. P. Leemans, Physics of Plasmas **14**, 056707 (2007), URL http://scitation.aip.org/content/aip/journal/pop/14/5/10.1063/1.2714022.

[7] J. Krall, G. Joyce, and E. Esarey, Phys. Rev. A **44**, 6854 (1991), URL http://link.aps.org/doi/10.1103/PhysRevA.44.6854.

[8] M. Shoucri, COMMUNICATIONS IN COMPUTATIONAL PHYSICS **4**, 703 (2008), ISSN 1815-2406, 20th International Conference on Numerical Simulation of Plasmas, Austin, TX, OCT 10-12, 2007.

[9] A. Grassi, L. Fedeli, A. Macchi, S. V. Bulanov, and F. Pegoraro, EUROPEAN PHYSICAL JOURNAL D **68** (2014), ISSN 1434-6060.

[10] T. Tajima and J. M. Dawson, Phys. Rev. Lett. **43**, 267 (1979), URL http://link.aps.org/doi/10.1103/PhysRevLett.43.267.

[11] J.-L. Vay, Phys. Rev. Lett. **98**, 130405 (2007), URL http://link.aps.org/doi/10.1103/PhysRevLett.98.130405.

[12] S. F. Martins, R. A. Fonseca, W. Lu, W. B. Mori, and L. O. Silva, Nat Phys **6**, 311 (2010), URL http://dx.doi.org/10.1038/nphys1538.

[13] J.-L. Vay, C. Geddes, E. Cormier-Michel, and D. Grote, Journal of Computational Physics **230**, 5908 (2011), ISSN 0021-9991, URL http://www.sciencedirect.com/science/article/pii/S0021999111002270.

[14] H. Ruhl and P. Mulser, Physics Letters A **205**, 388 (1995), ISSN 0375-9601, URL http://www.sciencedirect.com/science/article/pii/037596019500596U.

[15] R. Liboff, *Kinetic Theory: Classical, Quantum, and Relativistic Descriptions*, Graduate Texts in Contemporary Physics (Springer New York, 2006), ISBN 9780387217758, URL https://books.google.com/books?id=iqASBwAAQBAJ.

[16] C. D. Decker and W. B. Mori, Phys. Rev. Lett. **72**, 490 (1994), URL http://link.aps.org/doi/10.1103/PhysRevLett.72.490.

[17] T. Katsouleas and W. B. Mori, Phys. Rev. Lett. **61**, 90 (1988), URL http://link.aps.org/doi/10.1103/PhysRevLett.61.90.

[18] J. B. Rosenzweig, Phys. Rev. A **38**, 3634 (1988), URL http://link.aps.org/doi/10.1103/PhysRevA.38.3634.

[19] Z. M. Sheng and J. Meyer-ter Vehn, Physics of Plasmas **4** (1997).

[20] C. B. Schroeder, E. Esarey, and B. A. Shadwick, Phys. Rev. E **72**, 055401 (2005), URL http://link.aps.org/doi/10.1103/PhysRevE.72.055401.

[21] R. M. G. M. Trines and P. A. Norreys, Physics of Plasmas **13**, 123102 (2006), URL http://scitation.aip.org/content/aip/journal/pop/13/12/10.1063/1.2398927.

[22] D. A. Burton and A. Noble, Journal of Physics A: Mathematical and Theoretical **43**, 075502 (2010), URL http://stacks.iop.org/1751-8121/43/i=7/a=075502.

[23] T. Coffey, Physics of Plasmas **17**, 052303 (2010), URL http://scitation.aip.org/content/aip/journal/pop/17/5/10.1063/1.3418351.

[24] S. V. Bulanov, T. Z. Esirkepov, M. Kando, J. K. Koga, A. S. Pirozhkov, T. Nakamura, S. S. Bulanov, C. B. Schroeder, E. Esarey, F. Califano, et al., Physics of Plasmas **19**, 113102 (2012), URL http://scitation.aip.org/content/aip/journal/pop/19/11/10.1063/1.4764052.

[25] S. Gordienko and A. Pukhov, Phys. Plasmas **12** (2005).

[26] B. Afeyan, F. Casas, N. Crouseilles, A. Dodhy, E. Faou, M. Mehrenberger, and E. Sonnendruecker, EUROPEAN PHYSICAL JOURNAL D **68** (2014), ISSN 1434-6060.

[27] A. J. Klimas, Journal of Computational Physics **50**, 270 (1983), ISSN 0021-9991, URL http://www.sciencedirect.com/science/article/pii/0021999183900670.

[28] J. W. Schumer and J. P. Holloway, Journal of Computational Physics **144**, 626 (1998), ISSN 0021-9991, URL http://www.sciencedirect.com/science/article/pii/S0021999198959253.

[29] B. Eliasson, Journal of Scientific Computing **16**, 1 (2001), ISSN 1573-7691, URL http://dx.doi.org/10.1023/A:1011132312956.

[30] B. Eliasson, Transport Theory and Statistical Physics **39**, 387 (2010), http://dx.doi.org/10.1080/00411450.2011.563711, URL http://dx.doi.org/10.1080/00411450.2011.563711.

[31] Mehrenberger, M., Steiner, C., Marradi, L., Crouseilles, N., Sonnendrucker, E., and Afeyan, B., ESAIM: Proc. **43**, 37 (2013), URL http://dx.doi.org/10.1051/proc/201343003.

[32] G. Delzanno, Journal of Computational Physics **301**, 338 (2015), ISSN 0021-9991, URL http:

//www.sciencedirect.com/science/article/pii/S0021999115004738.

[33] A. J. Klimas and J. Cooper, Physics of Fluids **26** (1983).

[34] C. Cheng and G. Knorr, Journal of Computational Physics **22**, 330 (1976), ISSN 0021-9991, URL http://www.sciencedirect.com/science/article/pii/002199917690053X.

[35] M. M. Shoucri, Physics of Fluids **22** (1979).

[36] J. Weickert, *Scale-Space Theory in Computer Vision: First International Conference, Scale-Space'97 Utrecht, The Netherlands, July 2–4, 1997 Proceedings* (Springer Berlin Heidelberg, Berlin, Heidelberg, 1997), chap. A review of nonlinear diffusion filtering, pp. 1–28, ISBN 978-3-540-69196-9, URL http://dx.doi.org/10.1007/3-540-63167-4_37.